



OPEN Fracture properties of dolomite and prediction of fracture toughness based on BP-ANN

Yu Guo¹, Dengkai Liu²✉, Junying Rao^{3,4}✉, Feifei Guo² & Yao Peng¹

In this study, based on the digital image correlation technique, three-point bending tests were conducted on dolomite semi-circular bending (SCB) specimens, and the fracture properties of the SCB specimens, including crack opening displacement, apparent fracture toughness (K_{If}) calculated using the initial crack length and true fracture toughness (K_{Ic}) calculated using the effective crack length, were investigated first. Then, two datasets were constructed, incorporating specimen size parameters (such as radius, span, and initial crack length), tensile strength and fracture toughness. Considering the impact of specimen size, three backpropagation artificial neural network (BP-ANN) models were developed, two for predicting K_{If} and one for K_{Ic} respectively. Finally, the size effect of fracture toughness was studied. The results show that nonlinearity is exhibited in the pre-peak load-crack opening displacement curve. The analysis about the evolution of crack opening displacement and strain concentration zone suggests that the nonlinearity observed before the peak could be attributed to the emergence and progression of cracks. The K_{Ic} of D-1 specimen ($1.86 \text{ MPa}\cdot\text{m}^{1/2}$) is significantly larger than the K_{If} ($1.08 \text{ MPa}\cdot\text{m}^{1/2}$), indicating that the fracture toughness estimated using the LEFM underestimates the inherent toughness of the rock. The trained BP-ANN models have good predictive and generalization performance. As the span and initial crack length of the specimen increase, a gradual decrease is observed in both K_{Ic} and K_{If} . Simultaneously, a progressive downward shift is noted in both the K_{If} - f_t and K_{Ic} - f_t curves.

Keywords Dolomite, Fracture properties, Fracture toughness, Digital image correlation, Artificial neural network

Fracture mechanics focuses on studying the initiation, propagation, and instability failure patterns of materials, and it has been extensively applied across various engineering domains^{1,2}. In rock engineering, the application of fracture mechanics primarily serves two distinct and contrasting objectives: 1) to prevent crack growth and maintain the structural integrity and safety of excavated rock structures, including tunnels and subway stations; 2) to explore methods that promote efficient crack propagation for the efficient extraction of resources like geothermal energy and shale gas. Regardless of the purpose, gaining insights into the fracture characteristics of rocks is crucial.

Dolomite is widespread in southwestern China, and the probability of encountering dolomite strata is very high during underground engineering projects such as tunnel excavation and subway construction. For example, the Jixin tunnel on the Chengdu-Kunming railway^{3,4} and the Fangjiawan tunnel in Shanxi province⁵ are both undergoing construction through dolomite strata. Understanding the fracture characteristics of dolomite is vital to guarantee the safety and stability of tunnels, subway stations, and other underground projects during construction and operation.

To determine the fracture properties accurately, many auxiliary techniques have emerged^{6–10}. Among them, the digital image correlation (DIC) technique is an advanced application within the field of particle tracking, where the tracking targets are sub-images with unique patterns¹¹. By comparing speckle patterns captured at different times by a high-speed camera, the specimen displacement and strain can be obtained^{12,13}. Due to this technique has the advantages of not requiring auxiliary optical devices, easy installation and operation of experimental equipment and the ability to accurately calculate the specimen deformation, it enjoys widespread adoption and is very popular in the study of material fracture mechanics^{14–19}.

¹School of Management, Guizhou University of Commerce, Guiyang 550014, China. ²School of Management Science and Engineering, Guizhou University of Finance and Economics, Guiyang 550025, China. ³Research Center of Space Structures, Guizhou University, Guiyang 550025, China. ⁴Guizhou Provincial Key Laboratory of Green Building and Intelligent Construction, Guiyang 550025, China. ✉email: liudk@mail.gufe.edu.cn; jyrao@gzu.edu.cn

Fracture toughness, reflecting the ability to resist crack propagation, is the widely used fracture parameter in rock engineering^{20,21}. Due to the tensile strength (f_t) being significantly lower than the compression strength for rock materials, the mode I fracture toughness is most common, and its use is most frequent. At present, various specimen configurations are employed to measure this fracture toughness, such as chevron bend²², short rod²², cracked chevron notched Brazilian disc^{23–26} and semi-circular bend (SCB)²⁷. Among the numerous specimen configurations available, the SCB specimen has the advantages of simple sample preparation and convenient testing procedures, making it widely used in rock^{28–31}, asphalt concrete^{32,33} and fiber-reinforced concrete^{34–37}. The mode I fracture toughness (K_{Ic}) of the SCB specimen can be calculated as follows^{27,31–37}:

$$\begin{cases} K_I = Y \frac{P\sqrt{\pi a}}{2RB} \\ Y = -1.297 + 9.516 \frac{S}{2R} - \left(0.47 + 16.457 \frac{S}{2R}\right) \frac{a}{R} + \left(1.071 + 34.401 \frac{S}{2R}\right) \left(\frac{a}{R}\right)^2 \end{cases} \quad (1)$$

where B , S and R represent the thickness, span and radius of the SCB specimens, respectively. For materials where fracture process zone (FPZ) can be neglected (such as silicate glasses), by substituting peak load (P_{max}) and initial crack length (a_0) into Eq. (1), the true fracture toughness (K_{Ic}) can be obtained. However, for materials where the FPZ cannot be neglected, substituting P_{max} and a_0 into Eq. (1) will only obtain the apparent fracture toughness (K_{If}), because when the load reaches P_{max} , the crack has already propagated, and the crack length is no longer equal to a_0 , but rather to a_c .

Currently, to determine K_{Ic} , there are mainly two methods for calculating a_c : 1) Using techniques such as the DIC and numerical simulations to determine a_c by observing the specimen deformation^{28,38}; 2) Obtaining a_c by solving the relationship between theoretical dimensionless compliance and experimental compliance^{29,30,39,40}. Although the methods for calculating K_{Ic} based on the SCB specimens are already available, there are only a few scholars to calculate K_{Ic} when they studied the fracture properties of rock materials^{28,38}. Scholars tend to calculate K_{If} of materials such as rock³¹, asphalt concrete^{32,33} and fiber-reinforced concrete^{34–37}, and have generally reached a consensus: the measured K_{If} ^{41–44} is size-dependent and has a strong relationship with f_t ⁴⁵.

It should be emphasized that scholars have conducted independent studies on the size effect of K_{If} and the relationship between K_{If} and f_t . Currently, there are no scholars to study the relationship between K_{If} and f_t considering the influence of specimen size. The possible reasons of which maybe are: 1) it is difficult and costly to obtain the samples in site. For example, it is nearly impossible to directly measure fracture toughness by obtaining a large number of rock samples through continuous sampling that meets experimental requirements⁴⁶. 2) the experimental process is complex. Not only are the tests for obtaining f_t required, but also those for calculating the fracture toughness of various specimen sizes. 3) it is difficult to select suitable data analysis techniques. This study will become simple if a data analysis technique can be selected that allows the use of previous data to construct a dataset including specimen size, f_t , and fracture toughness, and to predict the fracture toughness.

Artificial neural network (ANN), as a data processing technique that rapidly developed in the 1980s, can directly study from examples, respond correctly or nearly correctly to incomplete tasks, generate generalizable results from new problems, and extract information from poor-quality or noisy data. Consequently, ANN has emerged as a highly powerful tool for solving numerous engineering problems, especially in cases where data is complex or insufficient. Over the past decade, ANN has been successfully applied in fields such as fracture mechanics of cement-based materials^{47–49}, prediction of material fracture toughness^{50–52}, material fatigue⁵³, and concrete technology^{54,55}.

In this study, based on the DIC technique, three-point bending (3-pb) tests were conducted on dolomite SCB specimens. Based on the data of the full-field deformation measured by the DIC, the calculation methods for mid-span deflection (δ_s) and crack mouth opening displacement (CMOD) were given, and the load–displacement curve, the evolution of crack opening displacement and strain concentration were investigated. Meanwhile, a comparison was made between two fracture toughness (K_{If} and K_{Ic}). In addition, by constructing two datasets using the diameter (D), span (S), initial crack length (a_0), tensile strength (f_t) and fracture toughness (K_{If} or K_{Ic}), three backpropagation artificial neural network (BP-ANN) models were established: two for predicting K_{If} and one for predicting K_{Ic} , all of which were utilized to analyze size-related variations in fracture properties.

Experimental program

Experimental materials

The rock samples were collected in Zhaotong City, Yunnan Province. To determine the sample type, X-ray diffraction (XRD) tests were employed on the samples. The analysis revealed that the mineral composition of the samples consisted of 85.2% dolomite, 13% calcite, and 1.8% quartz. Which confirmed that the collected rock samples are dolomite. The elastic modulus (E) of those samples is about 67.71 GPa.

The ISRM-suggested geometries for SCB specimens specify several key dimensions. Firstly, the specimen thickness (B) must be larger than $0.8R$, where R represents the specimen radius. Secondly, the initial crack length (a_0) should range from $0.4R$ to $0.6R$. Lastly, the distance between support points (S) needs to be between R and $1.6R$. Therefore, the collected samples were designed as semi-circular disks. The specimens including the initial cracks were made using waterjet cutting, and the specimen size is shown in Table. 1.

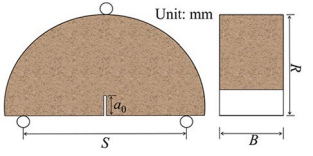
Specimen no	R (mm)	B (mm)	S (mm)	a_0 (mm)	P_{\max} (kN)	Schematic of the specimens
D-1	34	27.2	44.2	7.88	3.73	
D-2	34	27.2	44.2	8.04	3.85	
D-3	34	27.2	44.2	11.77	3.25	

Table. 1. Specimen size.

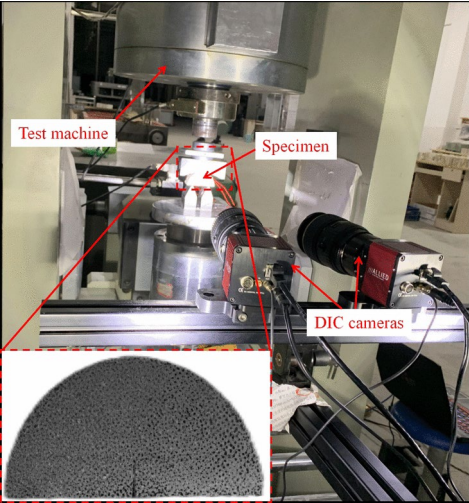


Fig. 1. Test setup.

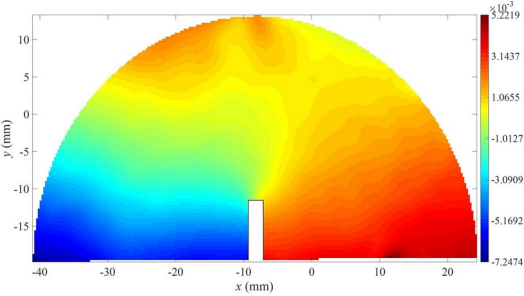


Fig. 2. Horizontal displacement contours.

Experimental process

Before conducting the tests, the surface of each specimen was treated by spraying speckles. After the speckle production was completed, the specimen was placed on the loading machine (RMT-301). The supports chosen were of the roller-in-groove type, with a roller diameter of 2 mm. Two DIC cameras (the camera resolution and frame rate are 4872×3248 pixels and 3 fps respectively) were positioned on the front side of the specimen to record the specimen deformation during the test. 3-pb tests were performed on the specimens at a loading rate of 0.0001 mm/s (see Fig. 1).

Experimental results

Deformation and crack propagation of specimen

The full-field horizontal displacement contour of the D-1 specimen at pre-peak 90% P_{\max} is shown in Fig. 2. Obviously, the left part of the specimen moves in the negative x -axis, while the right part moves in the positive x -axis. This indicates that as the test process, the crack in the specimen are gradually widening.

Taking the D-1 specimen as an example, the trajectory of the crack propagation is shown in Fig. 3. Obviously, the crack emerges from the initial crack tip and extends toward the loading point. However, the crack did not propagate straight up along the plane of the initial crack. This is mainly because the rock material is heterogeneous,

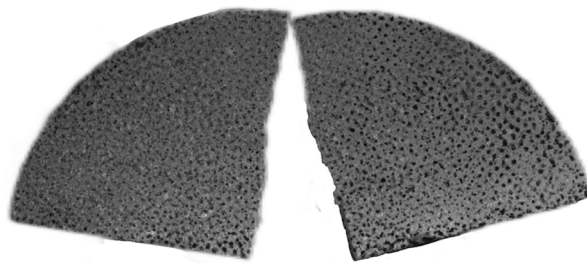


Fig. 3. Trajectory of the crack propagation.

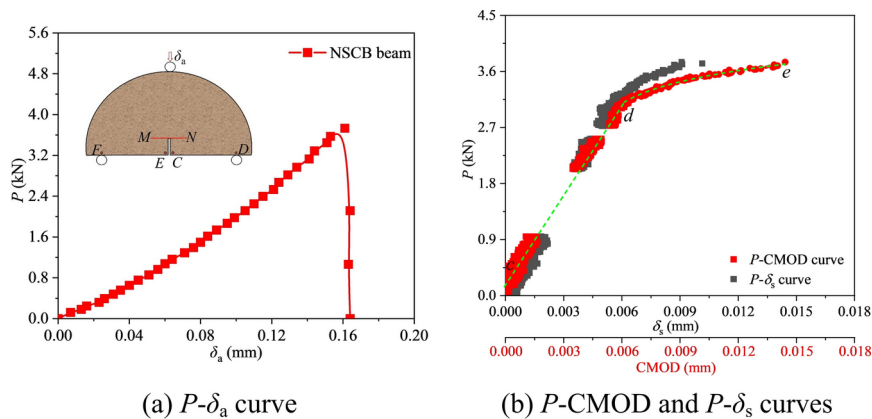


Fig. 4. Load-displacement curves, (a) P - δ_a curve, (b) P -CMOD and P - δ_s curves.

and the strengths of different mineral particles are different. Therefore, the crack tends to bypass the mineral particles with higher strength and propagate in a wavy pattern. After the peak, the crack rapidly develops, and the specimen suddenly fractures, indicating that the dolomite specimens are brittle, and the 3-pb tests of the SCB specimens do not provide good control over crack propagation.

Load-displacement curves

Measuring the CMOD and δ_s is a challenge by arranging sensors on the specimen surface, given their small size. Therefore, scholars tend to obtain the relationship between the actuator displacement (δ_a) and applied load (P). Figure 4a displays the P - δ_a curve of the D-1 specimen. At the pre-peak stage, the P - δ_a curve is not linear. The slope appears to increase slightly as the test progresses. This may be due to insufficient contact between the specimen and the loading equipment, as well as between the specimen and the supports during the initial stages of loading. When the load reaches the peak point, it suddenly drops vertically. This phenomenon occurs in both sandstone⁵⁶ and granite⁵⁷.

Utilizing the DIC allows for the determination of CMOD by computing the difference in horizontal displacement between two specified points, which are located at each side of the initial crack tip (see points C and E on the SCB specimen in Fig. 4a):

$$CMOD = u_C - u_E \quad (2)$$

The P -CMOD curve of the D-1 specimen, displayed in Fig. 4b, demonstrates the correlation between the actual specimen deformation and load. Unlike the P - δ_a curve, a nonlinear segment (d - e segment) was observed in the pre-peak P -CMOD curve. It appears that the specimen starts to crack at point d , and then the crack stable propagates until it reaches point e (i.e. the peak point), whereupon the specimen undergoes rapid failure.

Based on the DIC technique, δ_s can be indirectly calculated by selecting four points on the specimen surface (such as the points B, C, E and F in Fig. 4a):

$$\delta_s = \frac{v_C - v_E}{2} + \frac{v_{C'} - v_{E'}}{2} \quad (3)$$

Figure 4b displays the P - δ_s curve of the D-1 specimen. The variation pattern of the P - δ_s curve is consistent with that of the P -CMOD curve, but it differs greatly from the variation pattern of the P - δ_a curve. This discrepancy arises because δ_a may be influenced by factors such as the gap between the support and the specimen, which prevents it from accurately reflecting the true specimen deformation.

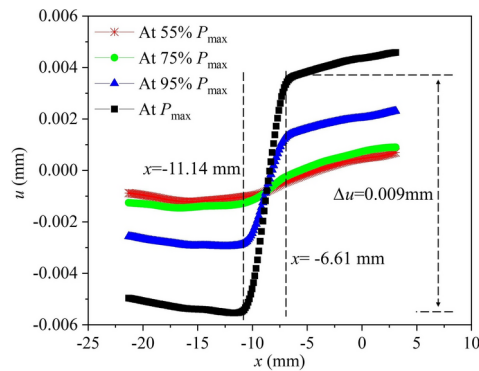


Fig. 5. Horizontal displacement along the line MN.

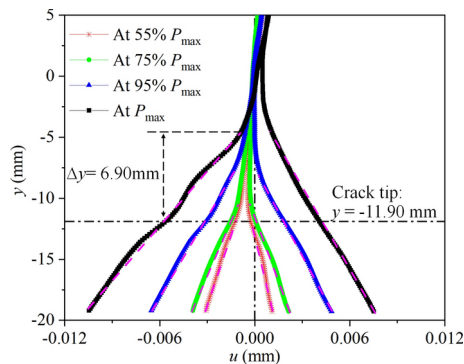


Fig. 6. Crack opening displacement along the y -axis.

Previous scholars generally believed that rock materials are in an elastic (linear) state before reaching the peak by analyzing the P - δ_a curve. However, this conclusion may have been misled by δ_a , which fails to accurately reflect the specimen deformation. In contrast, the variation patterns of the P -CMOD and P - δ_s curves indicate that there is a nonlinear segment in rock materials before reaching the peak. In the subsequent analysis, we attempt to explain the reasons for this nonlinearity through an analysis of the strain and displacement fields.

Crack opening displacement

The horizontal displacement at the initial crack tip along the line MN (see Fig. 4a) was extracted using the DIC, as displayed in Fig. 5. When a relatively small load (such as pre-peak 55% P_{\max}) was applied to the specimen, a linear change in horizontal displacement was observed along the line MN, suggesting that the specimen is undergoing elastic deformation. At pre-peak 95% P_{\max} , a noticeable displacement jump occurs, suggesting that a crack has formed. At P_{\max} , the horizontal displacement jump becomes more significant, indicating that the crack has propagated upwards.

Measuring crack tip opening displacement at the peak (CTOD_c) is crucial as it provides insights into the local failure characteristics⁵⁸. As shown in Fig. 5, CTOD_c of the SCB specimen can be determined by measuring the displacement difference between the points located at approximately ± 2.27 mm from the crack tip (from $x = -11.14$ mm to $x = -6.61$ mm), and this value is about 0.009 mm. Lin et al.⁵⁹ also determined CTOD_c within a range of approximately ± 2 mm from the crack tip, whereas Ji et al.⁵⁸ conducted their measurements within a narrower range of approximately ± 1 mm. The above analysis shows that when calculating crack tip opening displacement, the selection of positions on both sides of the crack needs to be determined based on the starting and ending points of the horizontal displacement jump.

By extracting the horizontal displacements of points on the vertical lines EG and CH (see Fig. 4a) located on both sides of the initial crack, the crack propagation can be assessed. As shown in Fig. 6, along the positive y -axis, the opening displacement gradually decreases. Compared to the opening displacement at pre-peak 55% P_{\max} , the opening displacement at P_{\max} is significantly larger, and the slope change point of the y - u curve shifts forward, indicating that the specimen has already cracked and the crack has propagated upwards.

Strain concentration zone

By observing the evolution of the full-field strain, the crack propagation also can be judged. According to the bilinear softening law^{60,61}, The strain threshold (ε_c) can be determined as follows:

$$\varepsilon_c = f_t/E \quad (4)$$

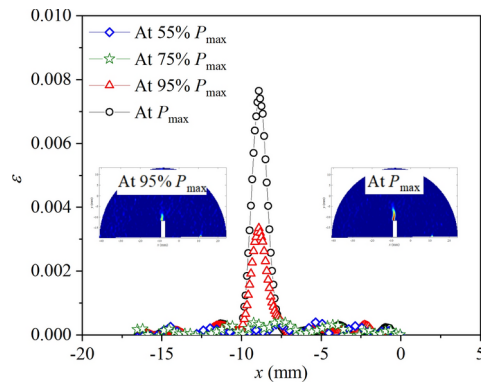


Fig. 7. Horizontal strain of D-1 specimen.

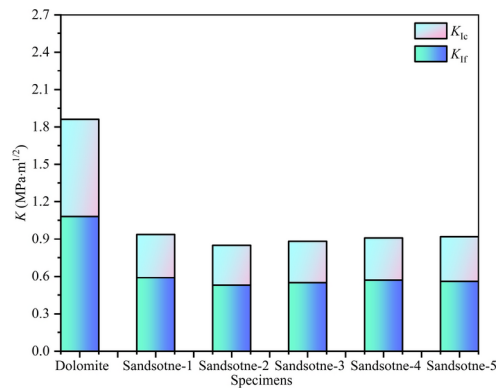


Fig. 8. Fracture toughness.

where f_t can be calculated as follows⁶²:

$$K_{If} = 0.125f_t \quad (5)$$

where K_{If} is the apparent fracture toughness, and it is about 1.10 MPa. By substituting K_{If} into Eq. (5), f_t can be obtained and is about 8.78 MPa. By substituting E and f_t into Eq. (4), ε_c can be obtained and is about 0.0001. Figure 7 displays the full-field strain of the D-1 specimen and the horizontal strains of points on the line MN. Obviously, as the test progresses, a strain concentration area starts to emerge and gradually extends upward, indicating that the specimen has cracked before reaching P_{max} . The strain concentration observed in the D-1 specimen at pre-peak 95% P_{max} is significantly stronger than that at pre-peak 75% P_{max} , indicating that the specimen has already cracked when the load is between 75% P_{max} and 95% P_{max} .

The aforementioned analysis shows that the crack initiated and progressed before reaching P_{max} , which is the likely main reason for the nonlinearity observed in the rock during this period.

Fracture toughness

(1) Based on theoretical derivation.

Figure 8 displays the K_{If} and K_{Ic} values for the D-1 specimen. Obviously, the K_{If} (1.08 MPa·m^{1/2}) is lower than the K_{Ic} (1.86 MPa·m^{1/2}), indicating that the fracture toughness estimated using the LEFM underestimates the inherent toughness of the rock. This underestimation arises because the crack initiated and propagated before reaching P_{max} . In addition, the K_{If} and K_{Ic} values of sandstone SCB specimens²⁸ were also plotted in Fig. 8, and consistent laws were found. The above findings indicate that using K_{Ic} is more accurate in practical engineering.

(2) Based on DIC and simulation techniques

Based on the full-field displacement measured by the DIC and simulation techniques, the stress intensity factor (SIF) of the dolomite specimens can also be obtained. The calculation process is shown in Fig. 9. Firstly, the DIC technique is employed to acquire the displacement field data of the target loading level (such as P_{max}). Subsequently, a numerical model is established based on the measured crack trajectory, and the displacement field data obtained by DIC is interpolated to obtain the displacement of each node in the numerical model.

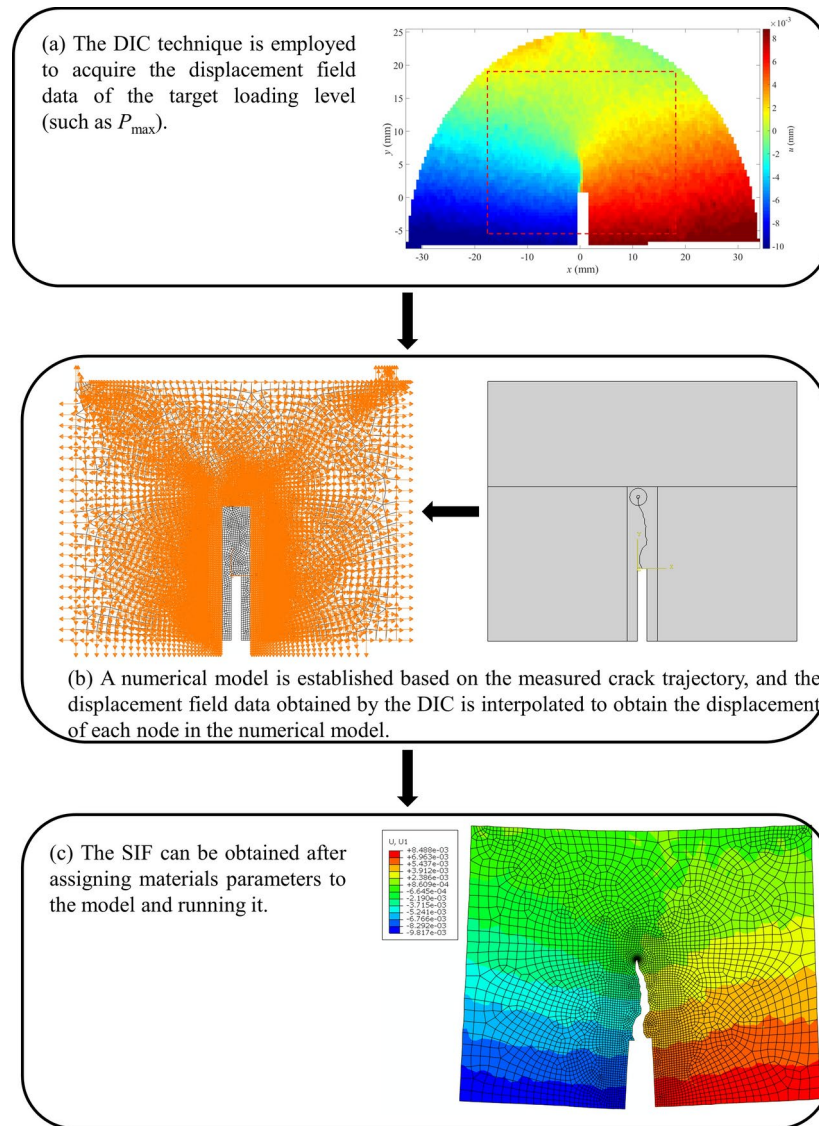


Fig. 9. Calculation process of the fracture process based on DIC and simulation techniques.

Finally, the SIF can be obtained using the contour integral method after assigning material parameters to the model and running it.

The numerical model has a length of 30 mm and a height of 24 mm, and it was considered to be an isotropic and homogeneous elastic material, with $E = 67.71$ GPa. Since the influence of Poisson's ratio on the calculation results of the model can be ignored⁶³, it is selected as 0.2 here. The model comprises 5176 nodes and 5078 elements. Specifically, within the contour integration area, the element type is CPS3 with a maximum element edge length of 0.3 mm; in other areas, the element type is CPS4R with a maximum element edge length of 1 mm.

The SIF of the D-1 specimen at the P_{\max} was calculated, which can be regarded as the fracture toughness. Due to the crack trajectory of the D-1 specimen not being a straight line but instead developing in a zigzag manner, there exists within the specimen not only Mode I fracture toughness (K_I) but also Mode II fracture toughness (K_{II}). The value of the K_I is about $2.20 \text{ MPa}\cdot\text{m}^{1/2}$, which has a 15.45% error compared to the K_{Ic} ($1.86 \text{ MPa}\cdot\text{m}^{1/2}$) calculated using Eq. (1). This indicates that the K_{Ic} calculated using Eq. (1) can represent the inherent toughness of rock materials. The reasons for this relatively large error between the K_I and K_{Ic} may be multifaceted, and two primary reasons are concluded as follows:

(1) Caused by the setting of the E in the model. Although the E used in the model is obtained through uniaxial compression tests (UCT), due to the significant discreteness of rock materials, there may be deviations between the E of specimens used for SCB tests and those used for UCT. When $E = 60.94$ GPa, $K_I = 1.98 \text{ MPa}\cdot\text{m}^{1/2}$, resulting in only a 6.06% error compared to the K_{Ic} .

(2) Caused by the tortuous propagation of the crack in the specimen. Due to the tortuous propagation of the crack, both the K_I and K_{II} exist in the specimen, and the fracture mode of the specimen can be regarded as a composite fracture. However, the use of Eq. (1) is based on the assumption that the crack is straight. The value

of the K_{II} is about $1.38 \text{ MPa}\cdot\text{m}^{1/2}$, indicating that the crack would continue to propagate, but its propagation direction would deviate from the initial crack direction.

Prediction of fracture toughness

Principles of the BP-ANN

The BP-ANN is a multi-layer neural network that employs the BP algorithm as its learning rule, exhibiting strong nonlinear mapping capabilities. It typically features an input layer, followed by one or several hidden layers and concludes with an output layer⁶⁴, as shown in Fig. 10. Each layer of the BP-ANN contains multiple neurons, and there are no connections among neurons within the same layer.

The training process of the BP-ANN consists of forward propagation (FP) stage and BP stage. During the FP stage, firstly, the neurons in the input layer transmit the input parameters to the neurons in the hidden layer. Subsequently, the neurons in the hidden layer compute the weighted sum of the received parameters, apply an activation function to this sum, and then pass the activated output to the neurons in the output layer. Ultimately, the neurons in the output layer compute the weighted sum of the received parameters, apply an activation function to this sum, and produce the final output of the network. In civil engineering, the widely used activation function, which can reflect the nonlinear characteristics of a problem, is as follows:

$$f_j = \frac{1}{1 + \exp\left(-\sum w_{nj}x_n + b_j\right)} \quad (6)$$

where w_{nj} represents a connection weight; b_j denotes a bias parameter. In the output layer, the actual output of the k^{th} neuron (g_k) can be obtained as follows:

$$g_k = \sum v_{jk}f_j \quad (7)$$

where v_{jk} represents a connection weight. After one forward propagation is completed, the mean squared error (MSE) is used to determine whether to terminate the training process. If the MSE falls below the target error, it signifies the completion of the training process, and the trained BP-ANN possesses predictive capabilities. Otherwise, the BP-ANN enters the BP stage. During this stage, the MSE is propagated backward along the original path, and the weights across all layers are updated to reduce the MSE. At present, the primary methods used for updating weights include the Levenberg–Marquardt (LM) and Bayesian Regularization (BR) algorithms. Since the BR algorithm demonstrates robust generalization capabilities when dealing with challenging, small, or noisy datasets, and the LM algorithm offers advantages such as reduced number of iterations, fast convergence speed, high accuracy, and strong robustness, these two algorithms were employed for training the established BP-ANN model.

Data handling process

1) Establish of dataset

Previous studies have shown that the diameter (D)^{41,42,65}, initial crack length (a_0)⁶⁶ and span (S)⁶⁷ of the SCB specimen can affect K_{Ic} while the thickness (B) has little influence on K_{Ic} ⁶⁶. To establish the BP-ANN model for predicting K_{Ic} that considers the influence of specimen size, a dataset (including D , a_0 , S , f_t and K_{Ic}) was established^{68–75} (see Table A.1 in Appendix). In addition, to establish the BP-ANN model for predicting K_{If} that considers the influence of specimen size, a dataset (including D , a_0 , S , f_t and K_{Ic}) was established^{28,68,76–79} (see Table A.2 in Appendix).

2) Establish of BP-ANN models.

Using the datasets presented earlier, two BP-ANN models (Models I and II) were established to predict K_{Ic} and K_{If} , respectively. It should be noted that although 174 and 59 sets of data are contained in Table A.1 and Table A.2 respectively, some data were randomly discarded when constructing Model I and Model II to prevent overfitting.

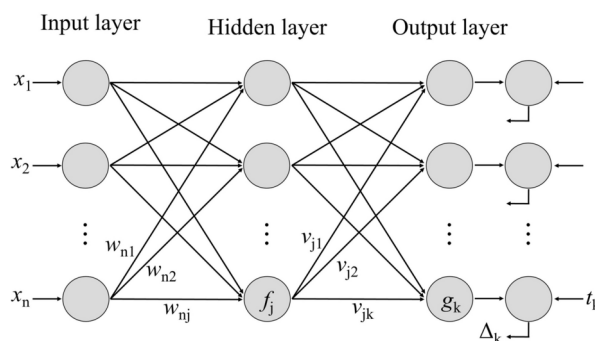


Fig. 10. Three-layer BP-ANN.

Before training the established models, it is necessary to normalize the data input into the model. In this study, the following formula was used for data normalization:

$$x_n^a = 0.1 + \frac{x_n^b - x^{\min}}{x^{\max} - x^{\min}} \times 0.8 \quad (8)$$

where x^{\max} and x^{\min} represent the maximum and minimum values of the selected vector before normalization, respectively; x_n^a and x_n^b represent the values before and after normalization, respectively.

The numbers of neurons in the input and output layers correspond to those of the input and output parameters. Therefore, when establishing the models, the numbers of neurons are set as 4 and 1, respectively. In addition, the hidden layers are set to a total of 1, since any engineering problem can be simulated effectively with a neural network that has one or two hidden layers^{48–50}. In the hidden layer, the calculation for the neurons goes as follows:

$$s = \sqrt{q + w} + \gamma_r \quad (9)$$

where γ_r is a random parameter, and $\gamma_r = 1 \sim 10$; w and q denote the counts of the neurons in the output and input layers, respectively; s denotes the counts of the neurons in the hidden layer, and is set as 4 in this study.

Training effect

When training the model I, the LM and BR algorithms were used. When using the BR algorithm, the training and test sets contained 85 and 36 sets of data, respectively. When using the LM algorithm, the training, validation, and test sets contained 85, 18, and 18 sets of data, respectively.

Figure 11 displays the training effect of model I based on the BR algorithm. The slope of the fitted curve in the training set is 0.98, and the error bar chart exhibits a characteristic of being higher in the middle and lower on both sides, indicating that the predicted and the target outputs are highly correlated. The slope of the fitted

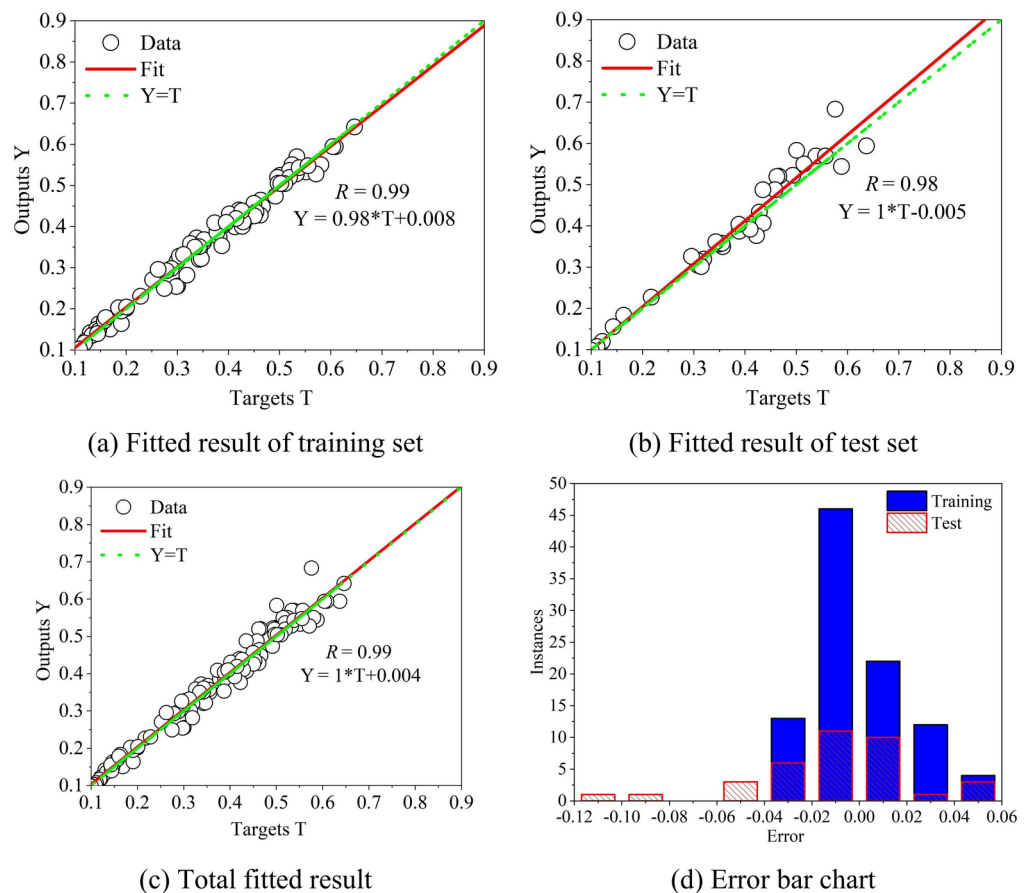


Fig. 11. Fitting effect and error based on the BR algorithm, (a) Fitted result of training set, (b) Fitted result of test set, (c) Total fitted result, (d) Error bar chart.

curve in the test set is 1.00, suggesting that the trained model has strong generalization performance. Since the slope of the fitted curve based on all data is also 1.00, it can be concluded that the model I trained using the BR algorithm possesses predictive capability.

Figure 12 displays the training effect of model I based on the LM algorithm. The slope of the fitted curve in the training set is 0.83, and the error bar chart exhibits a characteristic of being higher in the middle and lower on both sides, indicating that the predicted output aligns closely with the target output. The slope of the fitted curve in the test set is 0.78, indicating that the trained model has good generalization performance. Since the slope of the fitted curve based on all data is also 0.82, it can be concluded that the model I trained using the LM algorithm possesses predictive capability.

When training the model II using the LM algorithm, the training, validation and test sets have 29, 15 and 15 sets of data, respectively, and the training effect is shown in Fig. 13. The slope of the fitted curve in the training set is 0.98, and the error bar chart exhibits a characteristic of being higher in the middle and lower on both sides, indicating a strong correlation between the predicted and target outputs. The slope of the fitted curve in the test set is 0.71, suggesting that the generalization ability of the trained model is moderate. This may be due to incomplete data or large data dispersion. However, since the slope of the fitted curve based on all data is 0.91, it can be considered that the trained model II has predictive capability.

Parameters analysis

Since K_{If} is size-dependent, the size effect of K_{If} was investigated using the trained model I, as shown in Fig. 14a. When S , a_0 and f_t remain constant ($S=84$ mm, $a_0=18.10$ mm, $f_t=7.00$ MPa), as D increases, K_{If} gradually increases. Similar phenomena have been observed by Zhang⁷⁵ and Ayatollahi⁸⁰ et al. when they study the fracture properties of rocks. This indicates that in small specimens, the FPZ has not fully developed, and it varies with changes in specimen size. When D , a_0 and f_t remain constant ($D=100$ mm, $a_0=18.10$ mm, $f_t=7.00$ MPa), as S increases, K_{If} gradually decreases. Similar phenomena have also been observed by Tutluoglu et al.⁷² when they study the fracture properties of rocks. When D , S and f_t remain constant ($D=100$ mm, $S=84$ mm, $f_t=7.00$ MPa), as a_0 increases, K_{If} gradually decreases. Zhang⁷⁵ and Zhao⁸¹ et al. have also observed similar phenomena in their studies on the fracture properties of rocks.

The impact of specimen size (including D , a_0 and S) on the K_{If} - f_t curve was investigated here. When D remains constant, K_{If} gradually increases as f_t increases, which is consistent with the conclusions drawn by Whittaker⁸², Bachers⁸³ and Zhang⁸⁴; as D increases, the K_{If} - f_t curve shifts upwards (see Fig. 14b). As S increases, the K_{If} - f_t curve shifts downwards (see Fig. 14c). As a_0 increases, the K_{If} - f_t curve shifts downwards (see Fig. 14d).

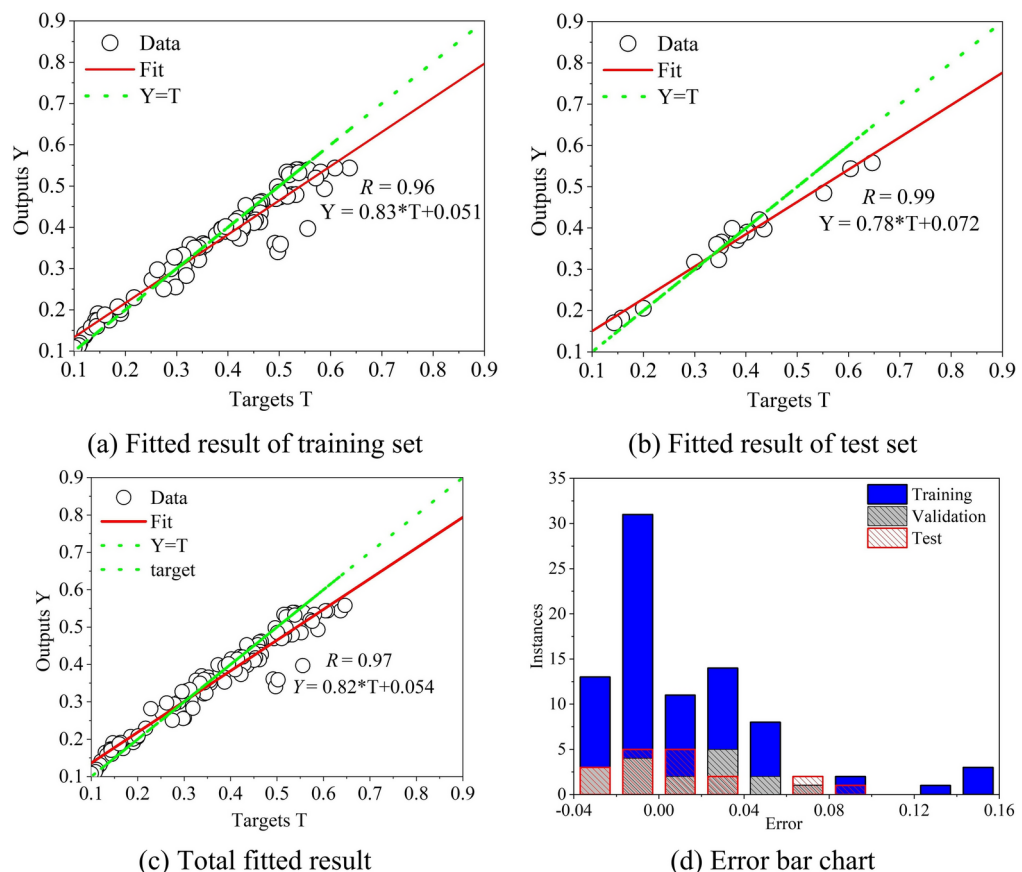


Fig. 12. Fitting effect and error based on the LM algorithm, (a) Fitted result of training set, (b) Fitted result of test set, (c) Total fitted result, (d) Error bar chart.

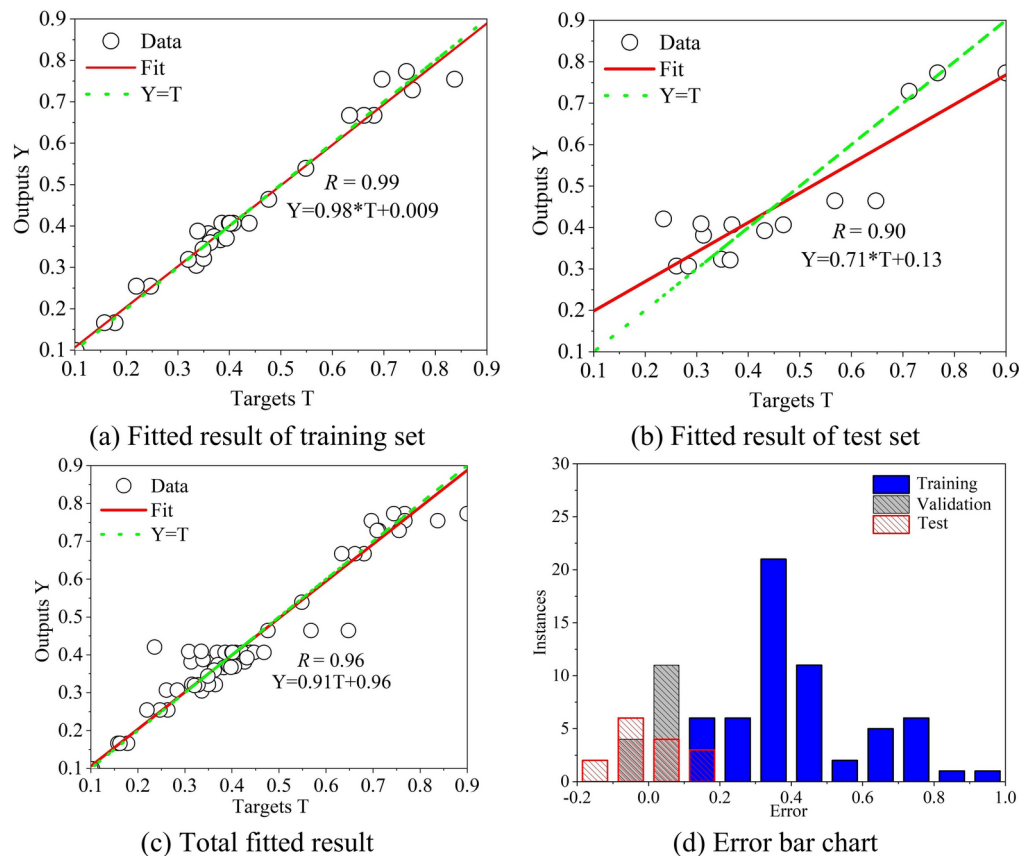


Fig. 13. Fitting effect and error based on the LM algorithm, (a) Fitted result of training set, (b) Fitted result of test set, (c) Total fitted result, (d) Error bar chart.

Figure 15a displays the size effect of K_{Ic} . When $S=50$ mm, $a_0=16$ mm and $f_t=7$ MPa, K_{Ic} increases with the increases of D . When $D=70$ mm, $a_0=16$ mm and $f_t=7$ MPa, K_{Ic} decreases with the increases of S . When $D=70$ mm, $S=50$ mm and $f_t=7$ MPa, K_{Ic} decreases with the increases of a_0 .

How the specimen size (including D , a_0 and S) influenced the K_{Ic} - f_t curve was investigated here. When $S=85.48$ mm and $a_0=18.90$ mm, as D increases, the K_{Ic} - f_t curve shifts upwards (see Fig. 15b). When $D=127.25$ mm and $a_0=18.90$ mm, as S increases, the K_{Ic} - f_t curve shifts downwards (see Fig. 15c). When $S=85.48$ mm and $D=127.25$ mm, as a_0 increases, the K_{Ic} - f_t curve shifts downwards (see Fig. 15d).

Using the BP-ANN to predict fracture toughness holds great potential. However, it should be noted that the tensile strength and fracture toughness within the same set of data in the dataset are mostly not obtained from the same specimen. Due to the significant randomness in the internal structure and defects of rock specimens, this may lead to variations in tensile strength and fracture toughness among different specimens. These variations will directly affect the quality of the dataset, and subsequently affect the prediction performance of the model. Additionally, the size of the dataset is also a crucial factor. If the dataset is too small, the prediction model may fail to converge effectively⁸⁵. Therefore, we must acknowledge that the accuracy of ANN model predictions heavily relies on the quality and size of the dataset.

Conclusions

In this study, based on the digital image correlation technique, dolomite specimens were tested, and the fracture properties of these specimens were investigated. Subsequently, apparent fracture toughness (K_{If}) and true fracture toughness (K_{Ic}) were predicted. The following are the main conclusions:

By analyzing the load-actuator displacement (P - δ_a) curve, previous studies believe that the rock remains in an elastic state before reaching the peak load (P_{max}). However, this conclusion may have been misled by δ_a , as it includes the gap between the specimen and its supports, and therefore fails to accurately reflect the specimen's deformation.

The pre-peak load-crack opening displacement curve exhibits nonlinearity. By analyzing both the crack opening displacement and strain concentration zone, it can be inferred that the nonlinearity observed before reaching the P_{max} may be attributed to the emergence and propagation of cracks.

K_{If} (calculated based on the initial crack length) is significantly lower than K_{Ic} (determined by considering the effect of crack propagation), indicating that the fracture toughness estimated using the LEFM underestimates the inherent toughness of the rock.

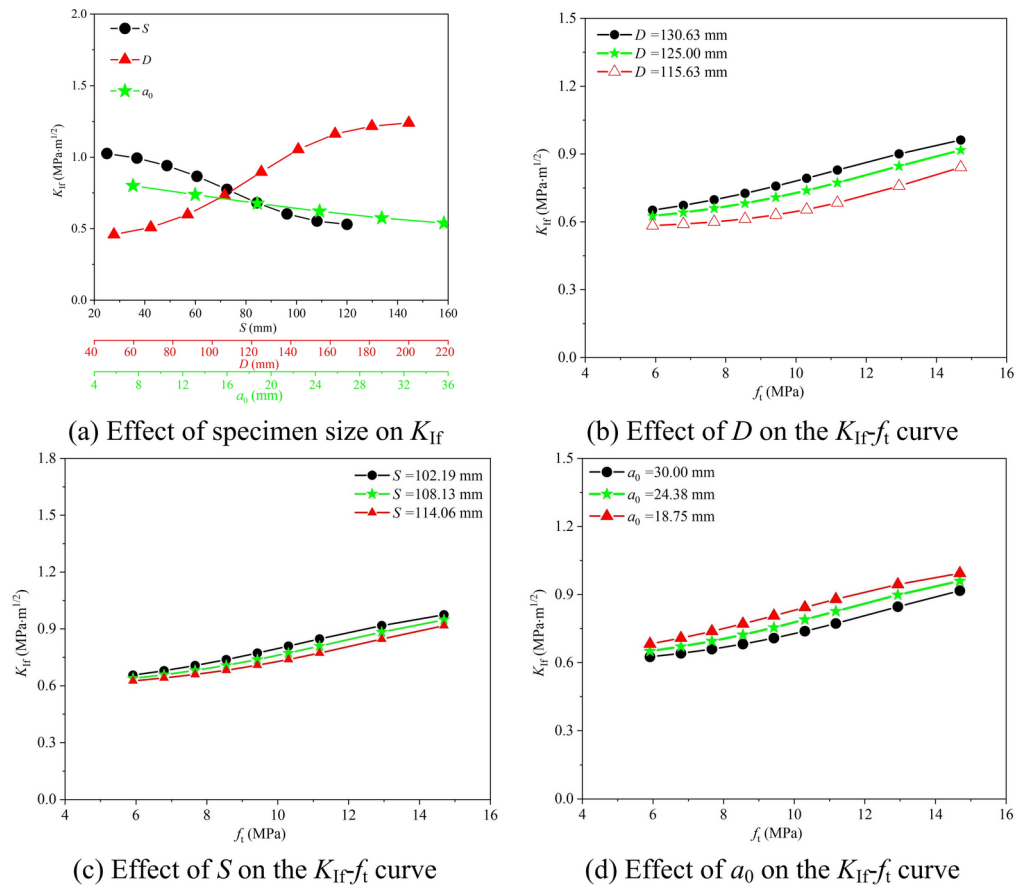


Fig. 14. Effect of geometric dimensions, (a) Effect of specimen size on K_{Ir} , (b) Effect of D on the K_{Ir} - f_t curve, (c) Effect of S on the K_{Ir} - f_t curve, (d) Effect of a_0 on the K_{Ir} - f_t curve.

After considering the size effect in establishing the BP-ANN models, the trained models demonstrated good predictive performance for both K_{Ir} and K_{Ic} , as well as strong generalization capabilities.

The trained models were used for parametric analysis, and the results show that as the span and initial crack length of the specimen increase, both K_{Ic} and K_{Ir} gradually decrease; while the K_{Ir} - f_t and K_{Ic} - f_t curves both shift downwards progressively.

Using the BP-ANN to predict the fracture toughness holds great potential. However, data dispersion arises because the tensile strength and fracture toughness values in the same set of data are not derived from identical specimens, due to potential variations in mechanical properties (such as these two parameters) across different specimens. This dispersion poses certain challenges for conducting this research using the BP-ANN.

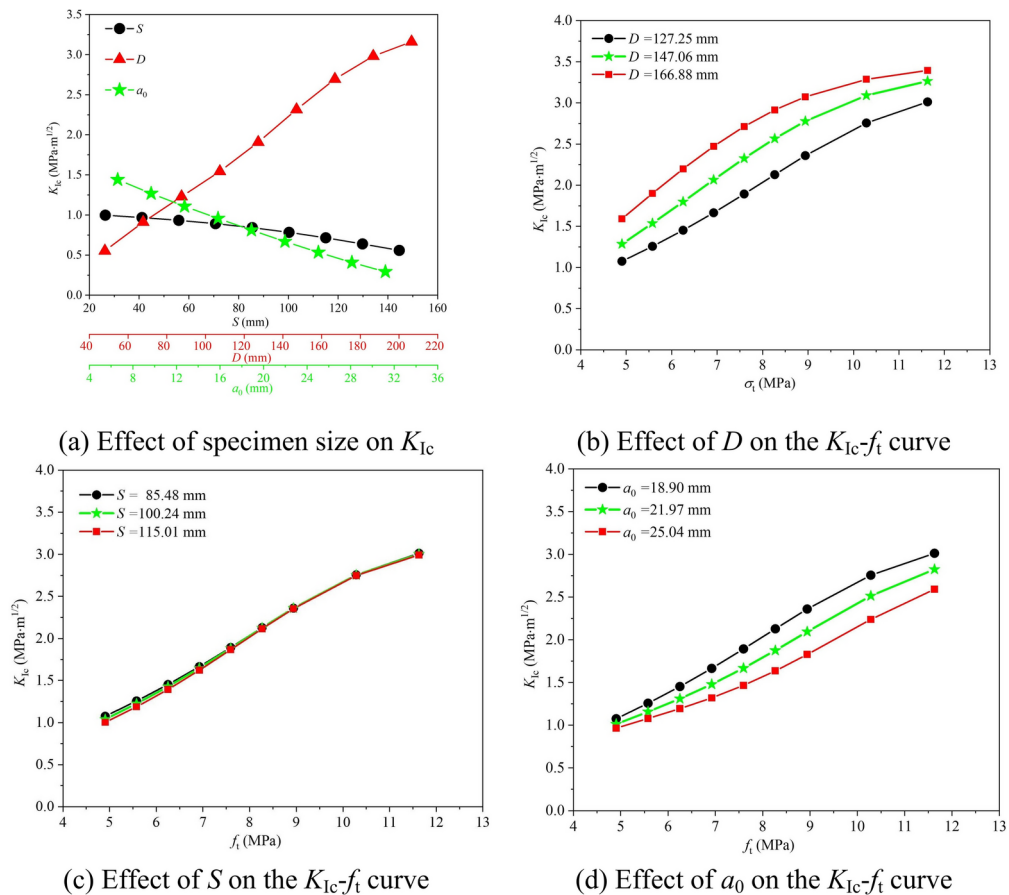


Fig. 15. Effect of geometric dimensions, (a) Effect of specimen size on K_{Ic} , (b) Effect of D on the K_{Ic} - f_t curve, (c) Effect of S on the K_{Ic} - f_t curve, (d) Effect of a_0 on the K_{Ic} - f_t curve.

Data availability

Data supporting the results of the study can be accessed upon reasonable request from the corresponding author.

Received: 6 December 2024; Accepted: 10 February 2025

Published online: 16 February 2025

References

- Fard, M. Y., Raji, B., Woodward, J. & Chattopadhyay, A. Characterization of interlaminar fracture modes I, II, and I-II of carbon/epoxy composites including in-service related bonding quality conditions. *Polym. Test.* **77**, 105894 (2019).
- Fard, M. Y., Raji, B. & Pankretz, H. Correlation of nanoscale interface debonding and multimode fracture in polymer carbon composites with long-term hygrothermal effects. *Mech. Mater.* **150**, 103601 (2020).
- Li J, Zhao W, Wang Z, Luo L, Mao B, Ju G. Study on the Effect of Advanced Drainage Length in Water - rich and Strong Sandy Dolomite Tunnel. *Railway Standard Design*. 1–11.
- Wang, Z. et al. Study on the mechanism of instability of tunnel face in sandy dolomite stratum. *Chin. J. Rock Mech. Eng.* **40**(S2), 3118–3126 (2021).
- Chen, X. & Song, Y. Research on dolomite karst treatment in fangjiawan tunnel of Xi'an-chengdu high speed railway passenger dedicated line. *Ch. Railw.* **02**, 11–16 (2021).
- Alam, S. Y., Saliba, J. & Loukili, A. Fracture examination in concrete through combined digital image correlation and acoustic emission techniques. *Constr. Build. Mater.* **69**(oct 30), 232–242 (2014).
- Hadjab, S. H., Chabaat, M. & Thimus, J.-F. Use of scanning electron microscope and the non-local isotropic damage model to investigate fracture process zone in notched concrete beams. *Exp. Mech.* **47**, 473–484 (2007).
- Muñoz-Ibáñez, A. et al. Pure mode I fracture toughness determination in rocks using a pseudo-compact tension (pCT) test approach. *Rock Mech. Rock Eng.* **53**(7), 3267–3285 (2020).
- Chen, H. H. & Su, R. Tension softening curves of plain concrete. *Constr. Build. Mater.* **44**(44), 440–451 (2013).
- Wu, Z., Rong, H., Zheng, J., Xu, F. & Dong, W. An experimental investigation on the FPZ properties in concrete using digital image correlation technique. *Eng. Fract. Mech.* **78**(17), 2978–2990 (2011).
- Fard, M. Y., Chattopadhyay, A. & Liu, Y. Nonlinear 3PB and 4PB flexural behavior and softening localization for epoxy resin E 863 using digital image correlation technique. *Exp. Tech.* **40**, 159–171 (2016).
- Chu, T., Ranson, W. & Sutton, M. A. Applications of digital-image-correlation techniques to experimental mechanics. *Exp. Mech.* **25**, 232–244 (1985).
- Sutton, M. A., Orteu, J. J. & Schreier, H. Image correlation for shape, motion and deformation measurements: basic concepts, theory and applications. Springer Science & Business Media (2009).

14. Roux, S., Réthoré, J. & Hild, F. Digital image correlation and fracture: an advanced technique for estimating stress intensity factors of 2D and 3D cracks. *J. Phys. D: Appl. Phys.* **42**(21), 214004 (2009).
15. Pan, B., Qian, K., Xie, H. & Asundi, A. Topical review: Two-dimensional digital image correlation for in-plane displacement and strain measurement: A review. *Meas. Sci. Technol.* **20**, 062001 (2009).
16. Nguyen, T. L., Hall, S. A., Vacher, P. & Viggiani, G. Fracture mechanisms in soft rock: Identification and quantification of evolving displacement discontinuities by extended digital image correlation. *Tectonophysics*. **503**(1–2), 117–128 (2011).
17. Shen, B. & Paulino, G. H. Identification of cohesive zone model and elastic parameters of fiber-reinforced cementitious composites using digital image correlation and a hybrid inverse technique. *Cem. Concr. Compos.* **33**(5), 572–585 (2011).
18. Leplay, P., Réthoré, J., Meille, S. & Baietto, M.-C. Identification of damage and cracking behaviours based on energy dissipation mode analysis in a quasi-brittle material using digital image correlation. *Int. J. Fract.* **171**, 35–50 (2011).
19. Lin, Q. & Labuz, J. F. Fracture of sandstone characterized by digital image correlation. *Int. J. Rock Mech. Min.* **60**, 235–245 (2013).
20. Wang, H., Liu, D., Cui, Z., Cheng, C. & Jian, Z. Investigation of the fracture modes of red sandstone using XFEM and acoustic emissions. *Theor. Appl. Fract. Mech.* **85**, 283–293 (2016).
21. Wang, H., Zhao, F., Huang, Z., Yao, Y. & Yuan, G. Experimental study of mode-I fracture toughness for layered shale based on two ISRM-suggested methods. *Rock Mech. Rock Eng.* **50**, 1933–1939 (2017).
22. Ouchterlony F. ISRM commission on testing methods. Suggested methods for determining fracture toughness of rock. *Int J Rock Mech Min Sci Geomech Abstr.* ;25(2): 71–96 (1988)
23. Iqbal, M. & Mohanty, B. Experimental calibration of ISRM suggested fracture toughness measurement techniques in selected brittle rocks. *Rock Mech. Rock Eng.* **40**, 453–475 (2007).
24. Fowell, R., Hudson, J., Xu, C. & Zhao, X. Suggested method for determining mode I fracture toughness using cracked chevron notched Brazilian disc (CCNBD) specimens. *Int. J. Rock Mech. Min. Sci. Geomech. Abstr.* **7**, 322A (1995).
25. Iqbal, M. & Mohanty, B. Experimental calibration of stress intensity factors of the ISRM suggested cracked chevron-notched Brazilian disc specimen used for determination of mode-I fracture toughness. *Int. J. Rock Mech. Min.* **43**(8), 1270–1276 (2006).
26. Wang, Q., Jia, X., Kou, S., Zhang, Z. & Lindqvist, P.-A. More accurate stress intensity factor derived by finite element analysis for the ISRM suggested rock fracture toughness specimen—CCNBD. *Int. J. Rock Mech. Min.* **40**(2), 233–241 (2003).
27. Kuruppu, M. D., Obara, Y., Ayatollahi, M. R., Chong, K. & Funatsu, T. ISRM-suggested method for determining the mode I static fracture toughness using semi-circular bend specimen. *Rock Mech. Rock Eng.* **47**, 267–274 (2014).
28. Wei, M., Dai, F., Xu, N., Zhao, T. & Xia, K. Experimental and numerical study on the fracture process zone and fracture toughness determination for ISRM-suggested semi-circular bend rock specimen. *Eng. Fract. Mech.* **154**, 43–56 (2016).
29. Yin, T., Wu, Y., Li, Q., Wang, C. & Wu, B. Determination of double-K fracture toughness parameters of thermally treated granite using notched semi-circular bending specimen. *Eng. Fract. Mech.* **226**, 106865 (2020).
30. Wu, Y., Yin, T., Zhuang, D., Li, Q. & Chen, Y. Research on the effect of thermal treatment on the crack resistance curve of marble using notched semi-circular bend specimen. *Theor. Appl. Fract. Mech.* **119**, 103344 (2022).
31. Yang, K., Zhang, F., Meng, F.-z., Hu, D.-w & Tan, X.-f. Effect of real-time high temperature and loading rate on mode I fracture toughness of granite. *Geotherm. Energy* **10**(1), 14 (2022).
32. Leon, L., Smith, J. & Frank, A. Intermediate temperature fracture resistance of stone matrix asphalt containing untreated recycled concrete aggregate. *Balt. J. Road Br. Eng.* **18**(1), 94–121 (2023).
33. Guo, Q. et al. Influence of basalt fiber on mode I and II fracture properties of asphalt mixture at medium and low temperatures. *Theor. Appl. Fract. Mech.* **112**, 102884 (2021).
34. Razmi, A. & Mirsayar, M. On the mixed mode I/II fracture properties of jute fiber-reinforced concrete. *Constr. Build. Mater.* **148**, 512–520 (2017).
35. Su, C., Wu, Q., Weng, L. & Chang, X. Experimental investigation of mode I fracture features of steel fiber-reinforced reactive powder concrete using semi-circular bend test. *Eng. Fract. Mech.* **209**, 187–199 (2019).
36. Aliha, M., Heidari-Rarani, M., Shokrieh, M. & Ayatollahi, M. Experimental determination of tensile strength and K (IC) of polymer concretes using semi-circular bend(SCB) specimens. *Struct. Eng. Mech.* **43**(6), 823 (2012).
37. Karimzadeh, H., Razmi, A., Imaninasab, R. & Esminejad, A. The influence of natural and synthetic fibers on mixed mode I/II fracture behavior of cement concrete materials. *Can. J. Civ. Eng.* **46**(12), 1081–1089 (2019).
38. Kramarov, V., Parrikar, P. N. & Mokhtari, M. Evaluation of fracture toughness of sandstone and shale using digital image correlation. *Rock Mech. Rock Eng.* **53**, 4231–4250 (2020).
39. Li, J., Du, Z.-W. & Guo, Z.-P. Effect of high temperature (600 °C) on mechanical properties, mineral composition, and microfracture characteristics of sandstone. *Adv. Mater. Sci. Eng.* **2020**, 1–19 (2020).
40. Xu, S., Malik, M. A., Li, Q. & Wu, Y. Determination of double-K fracture parameters using semi-circular bend test specimens. *Eng. Fract. Mech.* **152**, 58–71 (2016).
41. Jeong, S. S., Nakamura, K., Yoshioka, S., Obara, Y. & Kataoka, M. Fracture toughness of granite measured using micro to macro scale specimens. *Proc. Eng.* **191**, 761–767 (2017).
42. Ghoul, S., Bahrami, B., Ayatollahi, M. R., Driesner, T. & Nejati, M. Introduction of a scaling factor for fracture toughness measurement of rocks using the semi-circular bend test. *Rock Mech. Rock Eng.* **54**(8), 4041–4058 (2021).
43. Ghasemi-Ghalebahman, A., Aghdam, A. A., Pirmohammad, S. & Niaki, M. H. Experimental investigation of fracture toughness of nanoclay reinforced polymer concrete composite: Effect of specimen size and crack angle. *Theor. Appl. Fract. Mech.* **117**, 103210 (2022).
44. Guo, Z., Li, J., Song, Y., He, C. & Zhang, F. The size effect and microstructure changes of granite after heat treatment. *Adv. Mater. Sci. Eng.* **2021**, 1–14 (2021).
45. Feng, G., Wang, X.-c., Kang, Y., Luo, S.-g & Hu, Y.-q. Effects of temperature on the relationship between mode-I fracture toughness and tensile strength of rock. *Appl. Sci.* **9**(7), 1326 (2019).
46. Liu, W. Evaluation Method and Application of Three-dimensional Fracability for Low Permeability Tight Sandstone Reservoirs (China University of Petroleum, 2022).
47. Arslan, A. & Ince, R. *The Neural Network-Based Analysis of Size Effect in Concrete Fracture* (1995).
48. Arslan, A. & Ince, R. The neural network approximation to the size effect in fracture of cementitious materials. *Eng. Fract. Mech.* **54**(2), 249–261 (1996).
49. Ince, R. Prediction of fracture parameters of concrete by artificial neural networks. *Eng. Fract. Mech.* **71**(15), 2143–2159 (2004).
50. Seibi, A. & Al-Alawi, S. Prediction of fracture toughness using artificial neural networks (ANNs). *Eng. Fract. Mech.* **56**(3), 311–319 (1997).
51. Kang, J., Choi, B. & Lee, H. Application of artificial neural network for predicting plain strain fracture toughness using tensile test results. *Fatigue Fract. Eng. M.* **29**(4), 321–329 (2006).
52. Partheepan, G., Sehgal, D. & Pandey, R. Fracture toughness evaluation using miniature specimen test and neural network. *Comp. Mater. Sci.* **44**(2), 523–530 (2008).
53. Genel, K. Application of artificial neural network for predicting strain-life fatigue properties of steels on the basis of tensile tests. *Int. J. Fatigue*. **26**(10), 1027–1035 (2004).
54. Topcu, I. B. & Saridemir, M. Prediction of properties of waste AAC aggregate concrete using artificial neural network. *Comp. Mater. Sci.* **41**(1), 117–125 (2007).
55. Parichatprecha, R. & Nimityongskul, P. Analysis of durability of high performance concrete using artificial neural networks. *Constr. Build. Mater.* **23**(2), 910–917 (2009).

56. Li, B., Huang, D. & Ma, W.-Z. Study on the influence of bedding plane on fracturing behavior of sandstone. *Yantu Lixue/Rock Soil Mech.* **41**(3), 858–868 (2020).
57. Huang, Y., Tao, R., Chen, X., Luo, Y. & Han, Y. Study on fracture behavior and thermal cracking evolution law of granite specimens After high temperature treatment. *Chin. J. Geotech. Eng.* 1–9.
58. Ji, W.-W., Pan, P.-Z., Miao, S.-T., Su, F.-S. & Du, M.-P. Fracture characteristics of two types of rocks based on digital image correlation. *Yantu Lixue/Rock Soil Mech.* **37**(8), 2299–2305 (2016).
59. Lin, Q., Yuan, H., Biolzi, L. & Labuz, J. F. Opening and mixed mode fracture processes in a quasi-brittle material via digital imaging. *Eng. Fract. Mech.* **131**, 176–193 (2014).
60. Hoover, C. G. & Bažant, Z. P. Cohesive crack, size effect, crack band and work-of-fracture models compared to comprehensive concrete fracture tests. *Int. J. Fract.* **187**(1), 133–143 (2014).
61. Li, D. et al. Experimental study on fracture and fatigue crack propagation processes in concrete based on DIC technology. *Eng. Fract. Mech.* **235**, 107166 (2020).
62. Xu, X., Wu, S., Jin, A. & Gao, Y. Review of the relationships between crack initiation stress, mode I fracture toughness and tensile strength of geo-materials. *Int. J. Geomech.* **18**(10), 04018136 (2018).
63. Ouagne, P., Neighbour, G. B. & Mcenaney, B. Crack growth resistance in nuclear graphites. *J. Phys. D App. Phys.* **35**(9), 927 (2002).
64. Yan, Y., Ren, Q., Xia, N., Shen, L. & Gu, J. Artificial neural network approach to predict the fracture parameters of the size effect model for concrete. *Fatigue Fract. Eng. M.* <https://doi.org/10.1111/ffe.12309> (2015).
65. Ghasemi-Ghalebahman, A., Akbardoost, J. & Ghaffari, Y. Evaluation of size effect on mixed-mode fracture behavior of epoxy/silica nanocomposites. *J. Strain Anal. Eng. Des.* **52**(4), 239–248 (2017).
66. Wang, J., Huang, S., Guo, W., Qiu, Z. & Kang, K. Experimental study on fracture toughness of a compacted clay using semi-circular bend specimen. *Eng. Fract. Mech.* **224**, 106814 (2020).
67. Xie, Q., Zeng, Y., Li, S., Liu, X. & Du, K. The influence of friction on the determination of rock fracture toughness. *Sci. Rep.* **12**(1), 7332 (2022).
68. Yang, L., Li, J., Lou, J. & Wang, X. Study on fracture characteristics of coal samples based on notched semi-circular bending tests. *J. Min. Saf. Eng.* **39**(05), 1041–1050 (2022).
69. Liang, H. & Fu, Y. Fracture properties of sandstone degradation under the action of drying–wetting cycles in acid and alkaline environments. *Arab. J. Geosci.* **13**, 1–8 (2020).
70. Li, E., Wei, Y., Chen, Z. & Zhang, L. Experimental and numerical investigations of fracture behavior for transversely isotropic slate using semi-circular bend method. *Appl. Sci.* **13**(4), 2418 (2023).
71. Dutler, N., Nejati, M., Valley, B., Amann, F. & Molinari, G. On the link between fracture toughness, tensile strength, and fracture process zone in anisotropic rocks. *Eng. Fract. Mech.* **201**, 56–79 (2018).
72. Tutluoglu, L., Batan, C. K. & Aliha, M. Tensile mode fracture toughness experiments on andesite rock using disc and semi-disc bend geometries with varying loading spans. *Theor. Appl. Fract. Mec.* **119**, 103325 (2022).
73. Siregar, A. P. N., Rafiq, M. I. & Mulheron, M. Experimental investigation of the effects of aggregate size distribution on the fracture behaviour of high strength concrete. *Constr. Build. Mater.* **150**, 252–259 (2017).
74. Aliha, M., Sistaninia, M., Smith, D., Pavier, M. & Ayatollahi, M. Geometry effects and statistical analysis of mode I fracture in gitting limestone. *Int. J. Rock Mech. Min.* **51**, 128–135 (2012).
75. Zhang, S. et al. Experimental study of size effect of fracture toughness of limestone using the notched semi-circular bend samples. *Rock Soil Mech.* **40**(05), 1740–1749+1760 (2019).
76. Zhao, G. et al. Influence of notch geometry on the rock fracture toughness measurement using the ISRM suggested semi-circular bend (SCB) method. *Rock Mech. Rock Eng.* **55**(4), 2239–2253 (2022).
77. Funatsu, T., Shimizu, N., Kuruppu, M. & Matsui, K. Evaluation of mode I fracture toughness assisted by the numerical determination of K-resistance. *Rock Mech. Rock Eng.* **48**, 143–157 (2015).
78. Zhang, S. et al. Experimental study on development characteristics and size effect of rock fracture process zone. *Eng. Fract. Mech.* **241**, 107377 (2021).
79. Miao, S., Pan, P., Hou, W., He, B. & Yu, P. Stress intensity factor evolution considering fracture process zone development of granite under monotonic and stepwise cyclic loading. *Eng. Fract. Mech.* **273**, 108727 (2022).
80. Ayatollahi, M. & Akbardoost, J. Size and geometry effects on rock fracture toughness: Mode I fracture. *Rock Mech. Rock Eng.* **47**, 677–687 (2014).
81. Zhao, Y., Gong, S., Jiang, Y. & Han, C. Characteristics of tensile strength and fracture properties of coal based on semi-circular bending tests. *Chin. J. Rock Mech. Eng.* **35**(06), 1255–1264 (2016).
82. Whittaker BN, Singh RN, Sun G. Rock fracture mechanics. Principles, design and applications. (1992).
83. Backers T. Fracture toughness determination and micromechanics of rock under mode I and mode II loading. GeoForschungsZentrum Potsdam (2005).
84. Zhang, Z. An empirical relation between mode I fracture toughness and the tensile strength of rock. *Int. J. Rock Mech. Min.* **39**(3), 401–406 (2002).
85. Ince, R. Artificial neural network-based analysis of effective crack model in concrete fracture. *Fatigue Fract. Eng. M.* **33**(9), 595–606 (2010).

Acknowledgements

The work described in this paper is supported by the Disaster Remote Sensing Prevention Workstation of the Academician Innovation Team in Guizhou Province (No. KXJZ[2024]006), Guizhou Office of Philosophy and Social Science (21GZQN07) and Guizhou Provincial Sciences and Technology Projects, ZK[2023] Basic 080.

Author contributions

Yu Guo: Methodology, Investigation, Data curation, Formal analysis, Visualization, Writing—Original Draft Dengkai Liu and Junying Rao: Conceptualization, Supervision, Funding acquisition, Writing—Review & Editing Feifei guo and Yao Peng: Investigation, Writing—Review & Editing.

Funding

The Disaster Remote Sensing Prevention Workstation of the Academician Innovation Team in Guizhou Province, KXJZ[2024]006, Guizhou Provincial Sciences and Technology Projects, ZK[2023] Basic 080, Guizhou Office of Philosophy and Social Science, 21GZQN07

Declarations

Competing interests

The authors declare no competing interests.

Additional information

Supplementary Information The online version contains supplementary material available at <https://doi.org/10.1038/s41598-025-89906-0>.

Correspondence and requests for materials should be addressed to D.L. or J.R.

Reprints and permissions information is available at www.nature.com/reprints.

Publisher's note Springer Nature remains neutral with regard to jurisdictional claims in published maps and institutional affiliations.

Open Access This article is licensed under a Creative Commons Attribution-NonCommercial-NoDerivatives 4.0 International License, which permits any non-commercial use, sharing, distribution and reproduction in any medium or format, as long as you give appropriate credit to the original author(s) and the source, provide a link to the Creative Commons licence, and indicate if you modified the licensed material. You do not have permission under this licence to share adapted material derived from this article or parts of it. The images or other third party material in this article are included in the article's Creative Commons licence, unless indicated otherwise in a credit line to the material. If material is not included in the article's Creative Commons licence and your intended use is not permitted by statutory regulation or exceeds the permitted use, you will need to obtain permission directly from the copyright holder. To view a copy of this licence, visit <http://creativecommons.org/licenses/by-nc-nd/4.0/>.

© The Author(s) 2025